High Temperature Coupling of IR Inactive C=C Mode in Complementary Metal Oxide Semiconductor Metamaterial Structure

*Dihan Hasan, Prakash Pitchappa, Chong Pei Ho, and Chengkuo Lee**

High temperature (up to 400 °C) coupling of infrared (IR) inactive >C=C< mode is reported in complementary metal oxide semiconductor (CMOS)-compatible refractory metamaterial filter and absorber structure by leveraging the carbon defects in tetraethyl orthosilicate obtained plasma enhanced chemical vapor deposition SiO_2 thin film. Here, the role of strain gradient induced dipole moment in high stress configuration on the activation of otherwise inactive >C=C< vibration at IR is confirmed. The unusual suppression of the transition is also observed in the absorber structure when the cavity mode strongly overlaps with it. Finally, 14 times better modulation of resonance spectrum is reported by such coupling in absorber configuration that supports thin film interference. The numerical and analytical study of the effect is found to be qualitatively in agreement with the experimental results. The study can set new paths toward more efficient design of spectrally selective thermophotovoltaic energy emitter at mid-IR and novel mechanism for high temperature sensing on the ubiquitous CMOS platform.

1. Introduction

Metamaterial-based optical structures referring to engineered material with properties not readily available in nature, are finding a multitude of applications in sensing,[1] solar and thermophotovoltaic energy conversion,[2,3] optical communication,[4] big data storage,[5] and all-optical computation.[6] Designer surface plasmons, commonly known as collective electron oscillations in periodic, subwavelength structures made of metal provide a large degree of freedom due to their dispersion for realizing the aforementioned applications in a broad wavelength range starting from the visible to microwave spectrum.[7–14] Thanks to the pioneering role of nanotechnology, complicated plasmonic architectures with multifunctionalities have been already demonstrated.[15–26] However, large scale application of plasmonic metamaterial is strongly dependent on both the scalability and repeatability of the fabrication process which can be reasonably ensured in CMOS technology. Very recently, CMOS fabricated designer optical structures have been reported to achieve high Q Fabry–Pérot resonance for gas sensing,[27,28] MEMS tunable metamaterials for terahertz communication,[29,30] and switchable mid-IR absorber[31] while relying on a fairly challenging process flow. A recent paradigm shift in the field of nanophotonic and metamaterial research is the increasing investigation of phonon modes in bulk and 2D form[32,33] especially in the mid-IR domain (3–8 μm), the primary motivation being arose by the low loss and multifunctional nature of these modes. Under CMOS consideration, such mode has been explored in SiO_2 thin film originating from the Si—O and Si—D vibration.[34] However, all infrared (IR) phonon modes in bulk form reported so far are intrinsically active with net dipole moment due to the polar nature of the dielectric and investigation into IR inactive modes with no net dipole moment needs to be carried out. On the other hand, due to the electrical characteristic of vibrations, the IR activity and Raman activity are complementary to each other, meaning an IR inactive mode becomes Raman active and vice versa.[35] One example of strongly IR inactive mode is the sp^2-hybridized >C=C< vibration.[36] Interestingly, such IR inactivity can be theoretically broken by causing asymmetry into the >C=C< bond and inducing the net dipole moment in the oscillator. Infrared observation of Raman-active G band and D band has been reported in fact by symmetry breaking in nitrogen doped amorphous carbon.[37] In this work, however, we consider carbon rich SiO_2 thin film obtained by tetraethyl orthosilicate (TEOS)-based chemical vapor deposition (CVD) and report unusual switching behavior of the >C=C< bands being strongly dependent on temperature. We further leverage such thermally induced asymmetry driven excitation of IR inactive mode in CMOS dielectric and couple it into the CMOS metamaterial structures as a means of thermal modulation of their resonance spectra. We

D. Hasan, Dr. P. Pitchappa, Dr. C. Pei Ho, Dr. C. Lee
Department of Electrical & Computer Engineering
National University of Singapore
4 Engineering Drive 3, Singapore 117576, Singapore
E-mail: elelc@nus.edu.sg
D. Hasan, Dr. P. Pitchappa, Dr. C. Pei Ho, Dr. C. Lee
Center for Intelligent Sensors and MEMS
National University of Singapore
4 Engineering Drive 3, Singapore 117576, Singapore
D. Hasan, Dr. P. Pitchappa, Dr. C. Pei Ho, Dr. C. Lee
NUS Suzhou Research Institute (NUSRI)
Suzhou Industrial Park, Suzhou 215123, P. R. China
Dr. C. Lee
Graduate School for Integrative Science and Engineering
National University of Singapore
119077, Singapore

DOI: 10.1002/adom.201600778

consider two state-of-the-art metamaterial configurations: filter and absorber and explore enhanced modulation in the absorber configuration being governed by the existing thin film interference.[38] Our detailed investigation into the different sets of material and optical origin of the effect clearly identifies the role of asymmetry induced excitation of the >C=C< mode on the observed modulation. Such modulation mechanism is reported for the first time in the literature and may possibly open up new paths toward efficient thermophotovoltaic energy harvesting and high temperature monitoring in rugged application based on metamaterials.

2. Background Concept, Fabrication, and Characterization

Figure 1a shows the schematic representation of the origin of carbon defects in the SiO_2 thin film obtained by plasma enhanced chemical vapor deposition (PECVD) using TEOS as the precursor which goes through a stoichiometric decomposition process to deposit the oxide thin film.[39] However, unreacted radicals of TEOS are often trapped by the structural defect and lead to the presence of C=C bonds in the micro-Raman spectrum as the wafer defect.[40] We leverage such defect to investigate the coupling of >C=C< vibration into metamaterial resonances at high temperature. As per the rule of mutual exclusion, for centrosymmetric molecules, the Raman active modes are IR inactive, and vice versa.[41] Such IR inactivity arises due to the absence of net transition moment (M) in the volume $d\,\tau$ defined as

$$\vec{M} \approx \int \psi_0 \vec{\mu} \psi_e \, d\tau \tag{1}$$

Here, ψ_0 and ψ_e are the wave functions of the ground state and excited state, respectively, and $\vec{\mu}$ is the dipole moment operator. Previously, applied pressure induced symmetry breaking is found to activate IR silent modes in C_{60} crystal, i.e., to yield the net transition moment.[42] A close connection between the symmetry breaking and strain gradient in inhomogeneous medium obtained from the thermal stress at high temperature is reported in ref. [43]. It is, therefore, possible to achieve net nonzero transition dipole moment in thin film under thermal stress for otherwise IR inactive modes. The spectral position of these modes can again be a strong function of temperature, molecular weight, and molecular composition.[44] Besides, crystal stress can approximately cause a

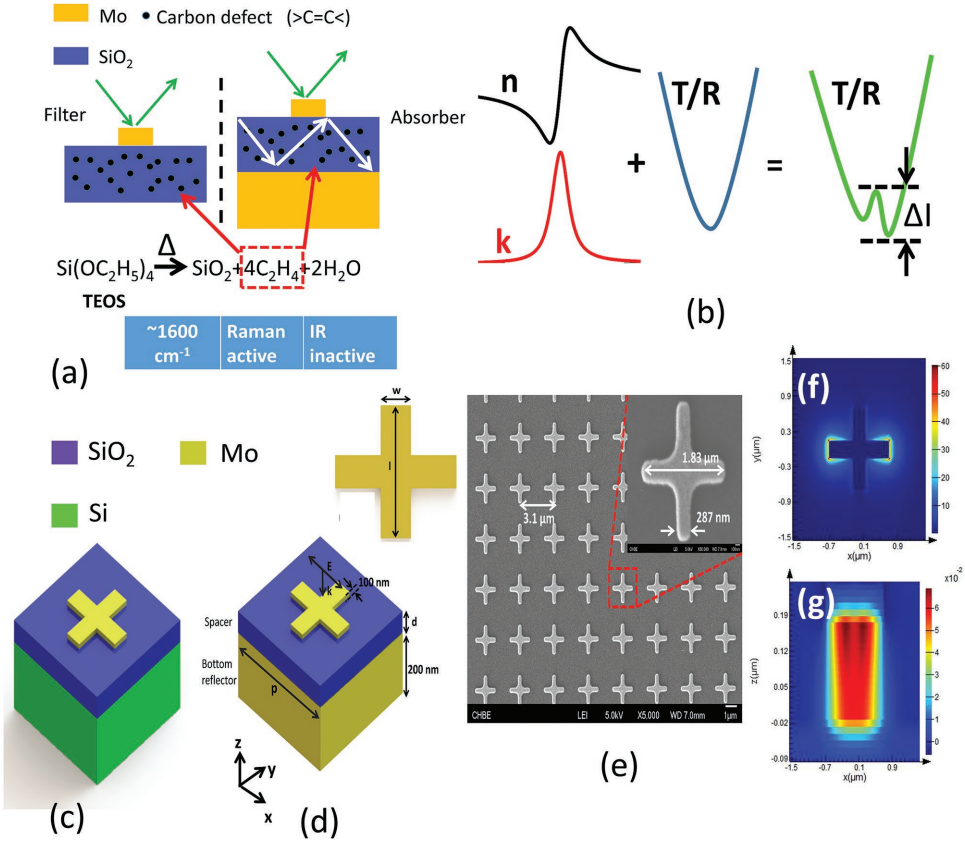

Figure 1. a) Schematic representation of the presence of carbon (>C=C<) defect in the SiO_2 layer. b) Conceptualization of the resonance modulation by coupling into >C=C< vibration. c), d) 3D schematic of the filter and absorber structure considered in this work, respectively. Inset: 2D layout of the cross-wire metamaterial pattern. e) FESEM image of the array of the patterns. Inset: zoomed in image of an unit cell. f) E-field distribution at the dipolar resonance of the pattern (period (p) 3.1 μm, length (l) 1800 nm, width (w) 287 nm, spacer (d) 200 nm. g) H-field intensity distribution across the cross section of the absorber geometry in panel (d). The intensity is mostly localized within the spacer region under maximum absorption condition. Incident polarization is along x-axis.

Table 1. Comparison of different metals for metamaterial structures.

Metal	Melting point [°C]	Electrical conductivity [$\times 10^7$ S m^{-1} @20 °C]	Plasma frequency [$\times 10^7$ Hz]	CTE [$\times 10^{-6}$ K^{-1}] (coefficient of thermal expansion)	Young's modulus (E [GPa])	CMOS compatibility
Aluminum	660	3.5	3.57	24	70	Yes
Gold	1000	4.52	2.2	14	78	No
Platinum	1770	0.944	1.25	8.8	168	No
Molybdenum	2620	1.9	1.8	4.8	329	Yes

linear shift of the vibrational frequency as given by $\Delta\nu = a_\sigma\sigma$ where σ is the stress and a_σ is the constant.[45] With these variables into consideration, we assume the position of the >C=C< mode to be localized around 1600 cm^{-1}.[41] We also employ the Drude–Lorentz type oscillator to model the vibration of the emitter.[46,47] Figure 1b shows the schematic presentation of the resonance modulation expected from the coupling between the metamaterial and >C=C< mode. Figure 1c,d shows the 3D schematic of the metamaterial filter and absorber structure, respectively. The 2D layout of the pattern is shown in the inset. FESEM image of the patterns is shown in Figure 1e. We employ the full wave FDTD solver to obtain the resonant field distribution of the geometries under x-polarization. The dipolar electric field distribution of the cross-wire pattern is shown in Figure 1f. H-field intensity distribution in Figure 1g across the device shows strong confinement in the absorber spacer region between the top metal patterns and the bottom metal reflector. Such confinement is in agreement with the spacer film interference of the absorber structure which is particularly absent in the filter structure.

In this work, we demonstrate the high temperature coupling behavior on a fully CMOS compatible refractory platform which can withstand the repeated heating cycles. Besides, we ensure large mismatch of coefficient of thermal expansion coefficient (TCE) between the metal and dielectric layer so as to maximize the strain gradient for IR excitation of the >C=C< signal. In our case, a combination of molybodenum (Mo) and SiO_2 gives the best mismatch of mechanical properties while both can sustain temperature up to 1000 °C in thin film form. **Table 1** is the comparison of Mo with other CMOS and nonCMOS candidates for metamaterial design at high temperature. **Table 2** lists the mechanical properties of the CMOS compatible dielectrics considered in this work. It is evident that, Mo-SiO_2 combination can yield the largest thermal stress while satisfying the all other conditions of refractory metamaterial platform based on CMOS technology.

2.1. Fabrication

A bare 8 in. silicon wafer was cleaned and 200 nm of Mo sputtering followed by the deposition of dielectric thin film for the spacer region and the top Mo film for the patterns were sputtered deposited under high vaccum. For the case of SiO_2 platform, PECVD was performed using TEOS as the precursor. For Al_2O_3, atomic layer deposition using tetramethylammonium hydroxide precursor was performed. High quality AlN thin film was obtained by sputtering. Deep UV photolithography process was used to define the metamaterial patterns. Finally, Mo was dry etched to form the final absorber and filter structure. In all cases, the thickness of the deposited dielectric is fixed at 200 nm.

2.2. Thin Film Characterization

First, we perform the confocal Raman spectroscopy to identify the presence of carbon bonds in the SiO_2 thin film. The laser wavelength is fixed at 532 nm. **Figure 2**a shows the Raman spectrum of 200 nm SiO_2 film deposited on Mo reflector. The translucent green rectangle indicates the locations of sp^2 carbon peaks, as observed in a graphitic system. The peak around 1000 cm^{-1} is due to the Si—O vibration. For reference, here we also provide the Raman spectrum of monolayer graphene on 300 nm PECVD oxide. The contrast between the G peak (1583 cm^{-1}) and D peak (1300 cm^{-1}) indeed indicates the high quality of the monolayer. We also observe the 2D peak at 2700 cm^{-1} in the monolayer graphene. In the case of PECVD SiO_2 on Mo, this peak shifts to 2500 cm^{-1}. We attribute this peak to the multiphonon lattice vibrational processes in the SiO_2 film. Overall, the presence of >C=C< peaks can be confirmed around the prescribed location (≈1600 cm^{-1}) from the Raman study. Figure 2c,d shows the strong characteristic peaks of the Al_2O_3 and AlN thin film, respectively. In these cases, no peaks corresponding to sp^2 hybridization are observed.

Table 2. Comparison of mechanical properties of the spacer material.

Material	Melting point [°C]	Young's modulus (E [GPa])	Poisson ratio [μ]	CTE [$\times 10^{-6}$ K^{-1}]	Thermal conductivity (K [W m^{-1} K^{-1}])
Aluminum nitride	2200	344.8	0.287	4.6	285
SiO_2	1600	70	0.17	0.5	1.4
Aluminum oxide	2072	353.1	0.22	4.5	25.08

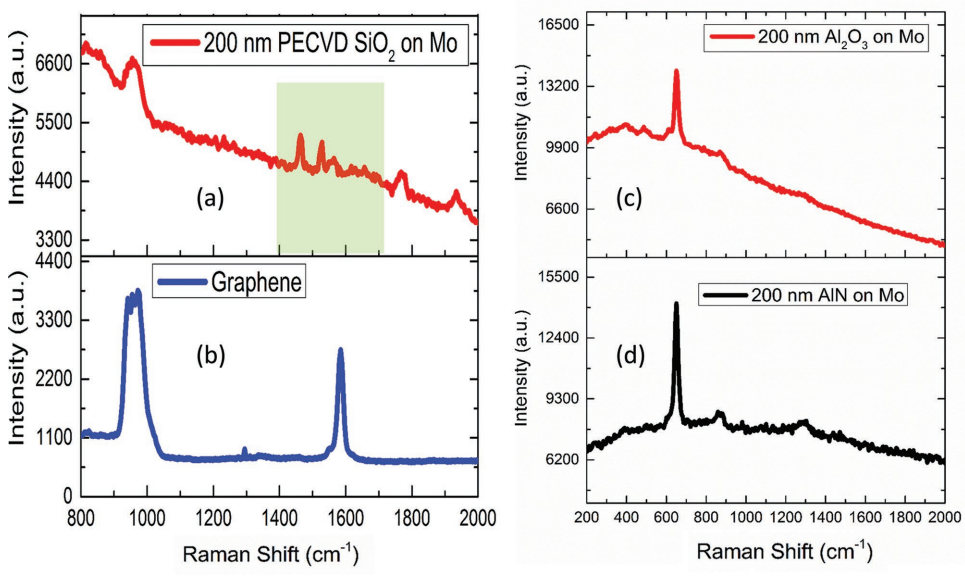

Figure 2. a) Confocal Raman spectroscopy of PECVD SiO_2 on Mo reflector. The translucent green rectangle indicates the presence of carbon peaks in the spectrum. b) Raman peaks of monolayer graphene on 300 nm SiO_2. c) Raman peak of atomic layer deposited Al_2O_3 on Mo reflector. d) Raman peak of sputter deposited AlN on Mo reflector.

Later, we perform the SEM-EDS investigation on the region without any metal pattern in order to quantify the amount of carbon within the finite volume of the freshly prepared and RCA cleaned thin film. The acceleration voltage is set at 15 KV and the signal was collected for 5 min. As shown in **Figure 3**, the wt% of carbon reaches 4.89% in the case of SiO_2 film (Figure 3c) and 3.88% for Al_2O_3 film (Figure 3a). The Mo signal and Si signal appearing in the spectra confirms the consideration of the total thin film volume during the analysis (Figure S1, Supporting Information). However, only 0.7% carbon signal could be detected in the case of sputter deposited AlN film. Note that, here, the at% of the carbon signal accounts for all possible covalent structures within the deposited thin films.

Figure 4a shows the IR spectra of 200 nm SiO_2 film on Si substrate as the temperature of the heat stage increases. The size of the collection aperture is fixed at 100×100 μm^2 throughout. Due to the symmetry of the patterns, no polarizer is used in the experiment. Reflection data are captured at 45° oblique incidence, whereas transmission data are obtained at normal incidence. Therefore, the P-polarization consists of both horizontal and vertical component during the reflection measurement. As indicated by the translucent grey rectangle and marked by the red dashed rectangle, a pronounced switching like behavior is observed when the temperature reaches 190 °C. Here, we define the switching by the origin of the dip as marked in the spectra. The transition retains without any further change as the temperature increases up to 400°. The contrast of the switching is found to be 5%. Interestingly, as the sample is cooled down to room temperature (25 °C), the IR spectrum returns to its original profile indicating the reversible nature of the process.

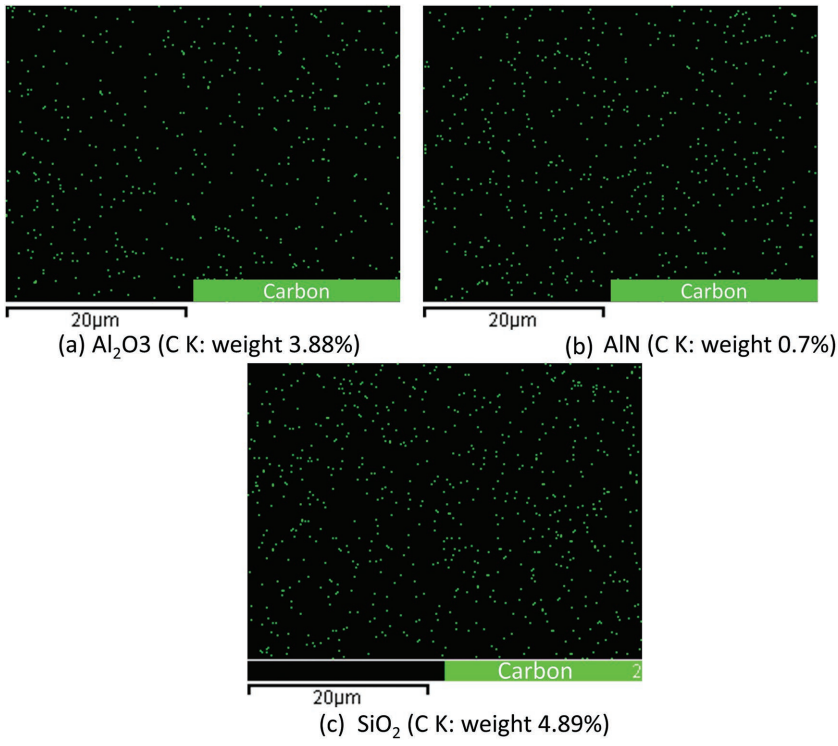

Figure 3. SEM-EDS mapping of carbon element a) 200 nm ALD deposited Al_2O_3 on Mo, b) 200 nm sputter deposited AlN on Mo, and c) 200 nm PECVD SiO_2 on Mo over an area of 40×40 μm^2.

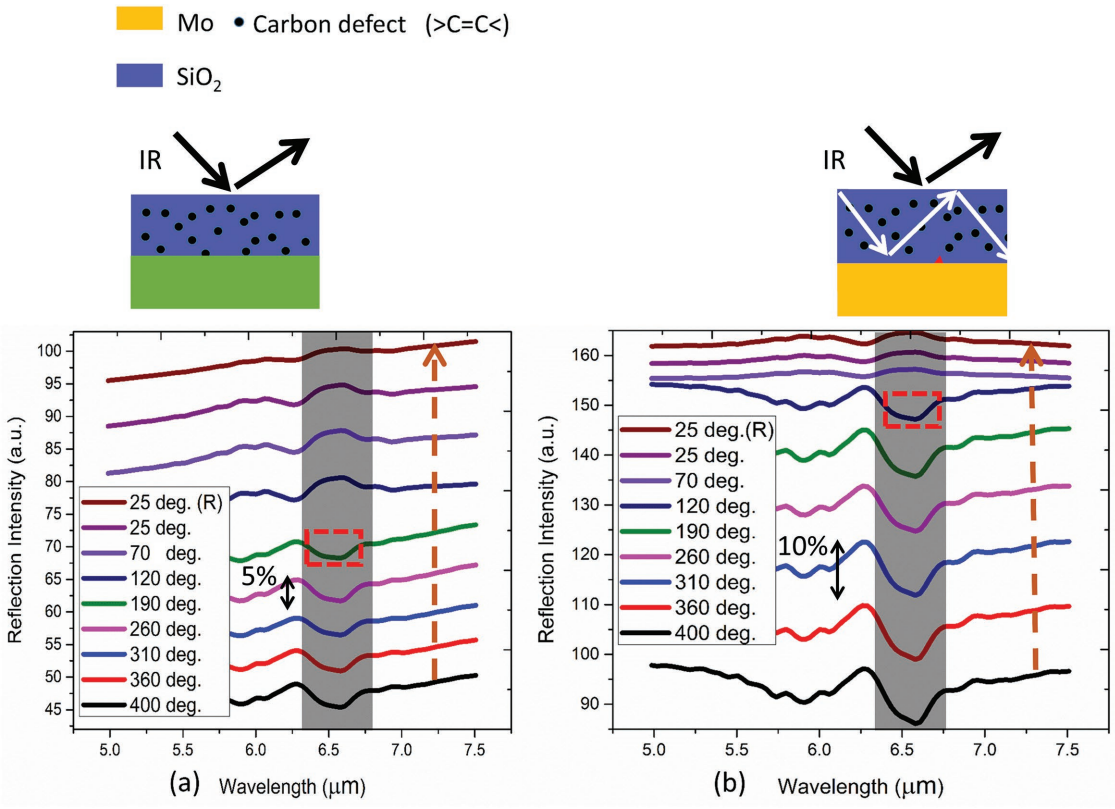

Figure 4. Activation of >C=C< mode in a) 200 nm SiO_2 on Si at 190 °C and b) 200 nm SiO_2 on Mo reflector at 120 °C as marked by the red dashed rectangle. The grey areas in the spectra indicate the region of interest. The orange dashed arrow implies the reversible nature of the transition as the samples are air cooled from 400 to 25 °(R). The solid black double arrow indicates the contrast of the switching.

We perform the similar experiment on the SiO_2 film deposited on Mo reflector in Figure 4b. Also in this case, a strong switching behavior is observed but at a lower temperature of 120 °C. The switching contrast in this is found to be 10%. Similarly, the reversible nature of the process is confirmed when the sample is cooled down to room temperature (25 °C). Considering the spectral location and vibrational nature of the >C=C< mode at room temperature, we attribute such transition to the activation of the IR inactive mode due to the partial breaking of the macroscopic symmetry in SiO_2 film as a result of large strain gradient at high temperature.[48] The strain gradient, being larger in the presence of Mo back metal film, the transition temperature is found to be lower in this case. The reversible nature of the process suggests the usefulness of the effect for repeatable applications.

3. Results and Analysis

3.1. Coupling in Filter Structure

Finally, we investigate the effect in two different metamaterial structures: filter and absorber. Here, the filter structure is a transmission filter based on 2D metamaterial layout with a 200 nm SiO_2 spacer, meaning a transmission dip in the spectrum when resonance occurs. Note that, in transmission mode, we do not observe any coupling of >C=C< mode in the absence of metamaterial patterns even when the oxide thickness is increased to 1 μm (Figure S2, Supporting Information). However, it is routinely observed in transmission signal in **Figure 5** and possibly indicates the coupling of energy between the broadband resonant mode and the narrowband emitter through the near electric field enhancement of the patterns at resonance. Note that, in all cases we focus on the feature corresponding to 6.3 μm as marked by orange arrow. This strongly correlates with the G peak of graphene at 1583 cm^{-1}. Any other spectral feature that may arise in the coupled system will be ignored for the sake of simplicity. In Figure 5, we increase the length (l) of the patterns by 100 nm and observe the coupling of the excited mode to the resonant mode of the metamaterial. Such variation allows us to sweep the resonance wavelength from 5 to 6.5 μm. In this investigation, the IR inactive mode is found to trigger at 200 °C in all cases (blue solid line). Besides, the quality factor of the resonant mode strongly deteriorates as the temperature increases due to the enhanced electron scattering in metal film and thermal stress[49,50] However, as the resonant mode overlaps with the emitter mode (C10), we observe a noticeable difference in resonance modulation. Nevertheless, the observed effect is much weaker (<1%) in comparison with the absorber structures, as discussed in the following section.

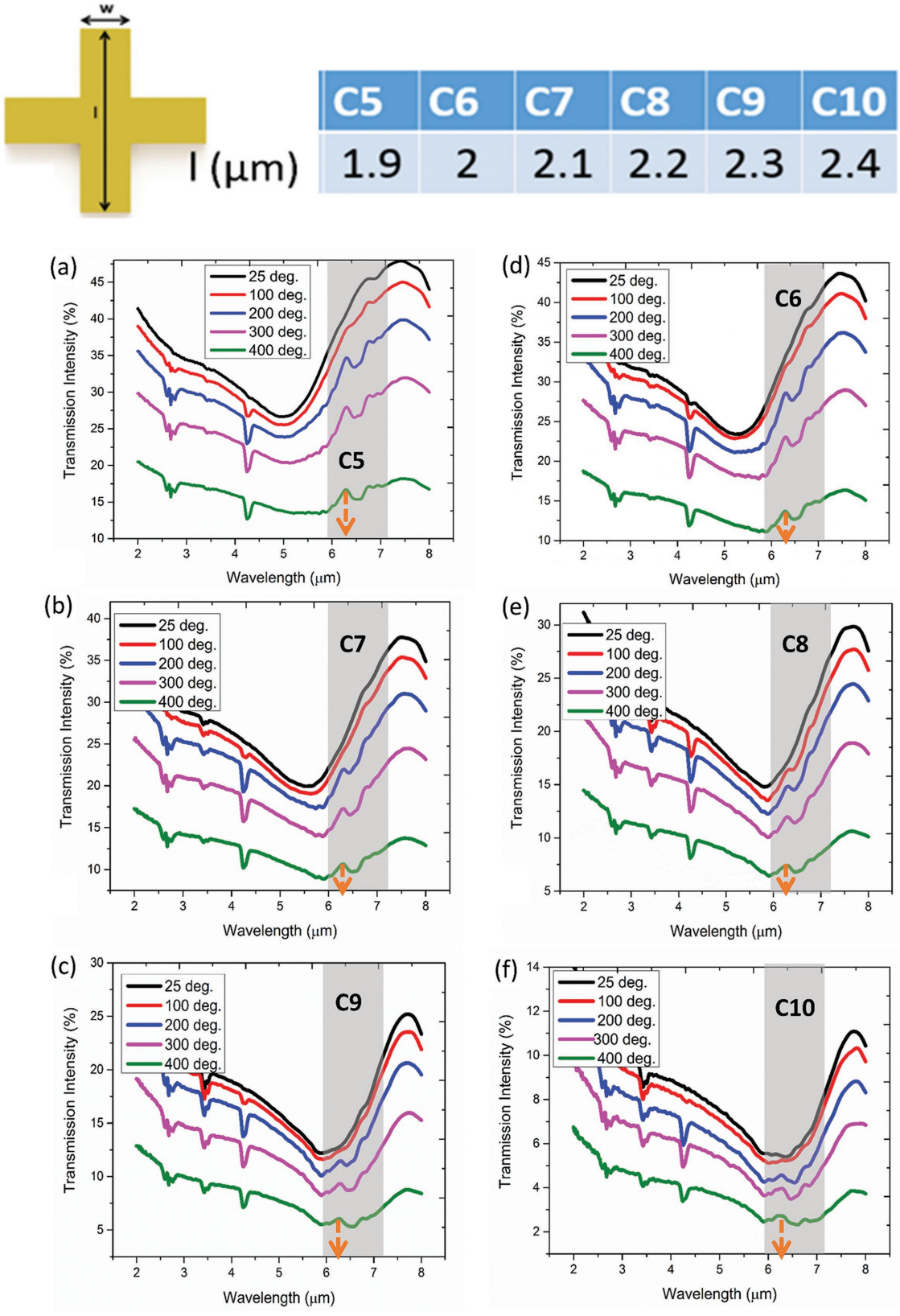

Figure 5. Transmission spectra as a function of temperature a) C5, b) C7, c) C9, d) C6, e) C8, and f) C10. The grey rectangle indicates the region of interest. The temperature dependent modulation of the transmission dip is found to vary as the dipolar resonance sweeps across the >C=C< vibration. The spectral feature at 6.3 μm under consideration is marked by the orange arrow.

3.2. Coupling in Absorber Structure

The absorber structure, due to its configuration, allows strong thin film interference as governed by the following equation[51]

$$\tilde{r} = \tilde{r}_{12} - \frac{\tilde{t}_{12}\tilde{t}_{21}e^{i2\tilde{\beta}}}{1+e^{i2\tilde{\beta}}\tilde{r}_{21}} \quad (2)$$

Here, the subscripts 1 and 2 denote the air and metal medium, respectively. $\tilde{r}$ and $\tilde{t}$ are the complex reflection and transmission coefficient at the air–metal interface and $\tilde{\beta}$ is the complex propagation constant in the dielectric spacer. Therefore, the absorption (A) defined as $1- |\tilde{r}|^2$. Based on the interference theory, any small optical change in the sub-wavelength spacer region can yield strong modulation of the reflection spectrum. In particular, the activation of the >C=C< mode in the spacer region should strongly interact with the absorption resonance of the structure.[52,53] **Figure 6** shows the variation of the reflection spectra as the length dimensions are varied from 1.9 to 2.4 µm (C5–C10). There are two important aspects to be noticed in this case. On the one hand, up to 200 °C, temperature dependence of the reflection dip is found to be a strong function of the resonance wavelength. As the length of the pattern is increased (C5–C10), the resonance wavelength red shifts. However, as marked in Figure 6, the intensity variation of the reflection dip remains quenched up to 200 °C when the resonance wavelength reaches 5.75 µm (C7) and beyond. This possibly occurs due to the dispersive nature of electron scattering even at elevated temperature. On the other hand, in all cases except C9 and C10, the >C=C< mode is found to be activated at 200 °C. In these two cases, full activation of the mode occurs only when the temperature reaches 400 °C. The observation is counterintuitive based on the experimental results in Figure 4b. We attribute this to the strong coupling between the metamaterial and the mode as the absorption resonance wavelength approaches the transition wavelength. The temporary suppression of the vibration signal from the emitter can be qualitatively explained by relating the decay rate to the inhomogeneous medium's Green tensor[46]

$$\Gamma = \Gamma_0 + \frac{2\tilde{\omega}_{21}^2}{\hbar\varepsilon_0 c^2} d_{21} Im G_s(r,r',\tilde{\omega}_{21}) d_{21} \quad (3)$$

Here, Γ_0 is the decay rate in free space, Gs is the Green tensor accounting for the anisotropy of the field distribution in the cavity structure, and d_{21} is the transition dipole moment. The $d_{21} Im G_s(r,r',\tilde{\omega}_{21}) d_{21}$ term is representative of the local density of states in the inhomogeneous medium. In contrast to the homogeneous and isotropic free space, the decay rate now becomes a function of the atomic position, field distribution, and the orientation of the transition dipole moment. Likewise in photonic crystal cavity, here we are observing a suppression of the spontaneous emission as the cavity mode of the metal-dielectric-metal structure overlaps with it. However, as the temperature is increased beyond 200 °C, we start to observe the appearance of the transition (C9) again. This perhaps occurs due to the detuning of the absorption resonance as a result of the heat induced permittivity change and intrinsic and extrinsic stress modification as no significant improvement of the signal strength is observed in Figure 4b after the switching occurs at 120 °C. The detuning is also associated with a large change of reflection intensity. Such heat induced effect is routinely observed in all the cases (C5–C10). It is reasonable to argue that the effect can strongly manipulate the local density of states of the emitter allowing it to emit again. As seen before in Figure 5, no such behavior in the cases of the transmission filter was noticed. In general, we observe strong coupling of the vibrational signal to the metamaterial resonance in the absorber structures. From the classical point of view, the resonance in absorber structure is purely magnetic in nature where the vibrational emitters are located within the dielectric cavity. Therefore, it has been possible to strongly tailor the vibrational mode by coupling. Detailed quantum mechanical investigation of this phenomenon can be performed in future.

It is also notable that, no strong resonance shift except resonance broadening is observed as the temperature is increased even at the maximum coupling condition. This indicates that the imaginary refractive index of the activated carbon is dominant over the real refractive index. The thermo-optic coefficient of SiO_2 is $+12.9 \times 10^{-6}$ per °C, and therefore any temperature induced refractive index change can be ignored at wavelengths far from the transition region. Besides, we observe no strong effect of temperature dependent metal permittivity possibly due to the large interfacial stress of the system. We further provide the data of the absorber structure when cooled down to room temperature and report very small change as compared to the case with no heating (Figure S3, Supporting Information).

3.3. Modeling of the Coupling of Vibrational Transition

We attempt to model the coupling of transition considering it as a Drude–Lorentz oscillation[47] defined as below

$$\varepsilon = \varepsilon_0 + \frac{p\omega_0^2}{\omega_0^2 - 2i\delta\omega - \omega^2} \quad (4)$$

Although no experimental data are available at current stage, the modeling will be useful for the intuitive understanding of the nature of coupling as the device dimension as varied. Here, ε_0 is the background permittivity fixed at 1.42, p is the strength of the oscillator fixed at 0.014. ω_0 is the transition frequency (wavelength) set at $2.99e + 14$ rad s^{-1} (6.3 µm). Indirectly, p refers to the filling fraction of the defects within the thin film. We assume the linewidth δ to be 1% of the transition frequency, i.e., $2.99e + 12$ rad s^{-1}. **Figure 7** shows the 2D color map (length versus wavelength) of the resonance profiles of the structures. As observed, a distinct peak around 6.3 µm appears both in the transmission (filter) and reflection (absorber) spectrum. We also observe a strong splitting in the absorber structure as the length of the pattern approaches the transition wavelength. Such splitting is not observable in the filter case. This again signifies the increased amount of

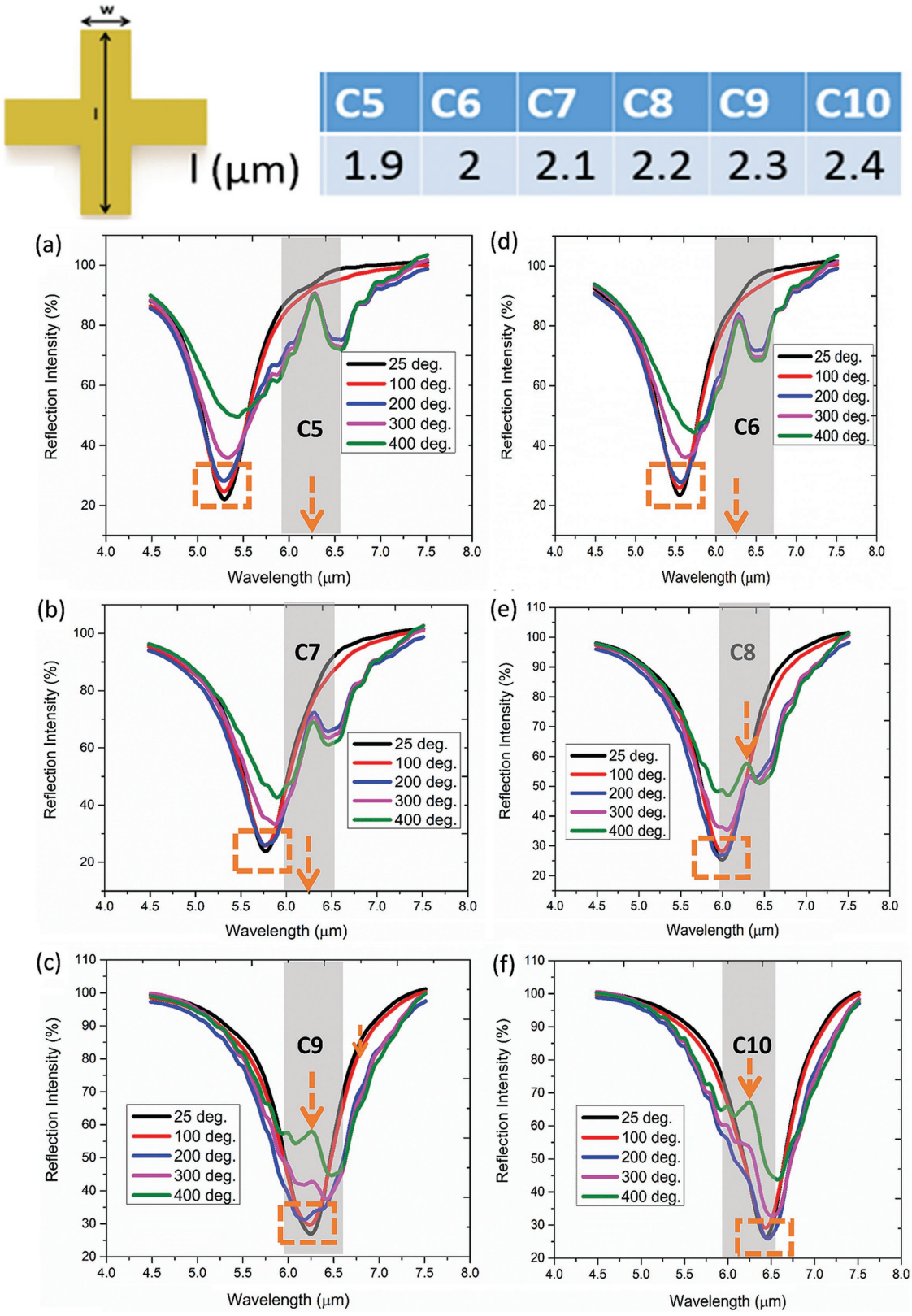

Figure 6. Reflection spectra as a function of temperature a) C5, b) C7, c) C9, d) C6, e) C8, and f) C10. The grey rectangle indicates the region of interest. Strong temperature dependent modulation of reflection dip is observed as the peak absorption wavelength approaches the >C=C< vibration line. The orange dashed rectangle indicates the wavelength dispersion of temperature dependence of the reflection dip intensity. The spectral feature at 6.3 μm under consideration is marked by the orange arrow.

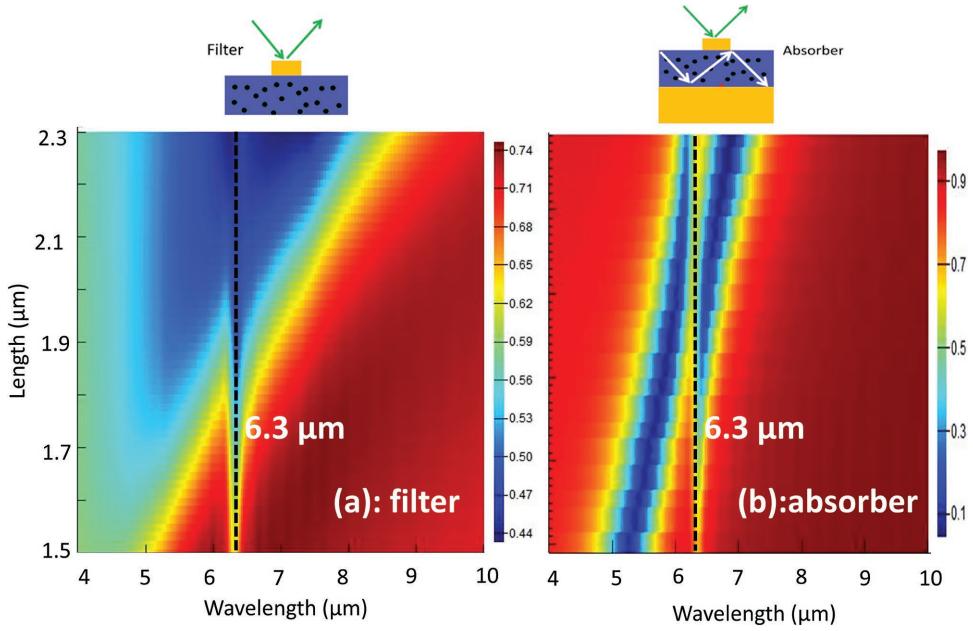

Figure 7. Simulated 2D color map (length versus wavelength) of the resonance spectra. a) Transmission in filter configuration and b) reflection absorber configuration. The >C=C< transition is defined at 6.3 μm. The strength of the oscillator is fixed at 0.014 in this case. The simulation ignores the heat induced effects, i.e., permittivity change and stress.

coupling of the vibrational transition in the absorber structure. Also note that, here, the simulation does not account the actual local density of states of the emitters in the inhomogeneous medium and therefore, cannot explain the suppression of the coupling as observed in the previous experimental results in Figure 6.

Furthermore, we deploy the following analytical equations derived from the normalized coupled mode theory[54]

$$\ddot{x}_1 + \Gamma\dot{x}_1 + \omega_1^2 x_1 + \kappa x_2 = a_1 \cos(\omega t) \tag{5}$$

$$\ddot{x}_2 + \gamma\dot{x}_2 + \omega_2^2 x_2 + \kappa x_1 = 0 \tag{6}$$

Here, (ω_1 Γ, a_1) are the metamaterial resonance, linewidth, and the amplitude of the driving force, respectively. (ω_2, γ) are the transition wavelength and the linewidth of the transition, respectively. The toy model is schematically shown in **Figure 8**a. The model allows to investigate the effect of increasing coupling coefficient (κ) on the modulation and lamb shift in the Fano system.[55] Coupling enhancement can be achieved by either changing the metamaterial configuration or increasing the concentration of the carbon defect. In a normalized system, we set the Γ and γ at 0.2 and 0.01, respectively, and observe the response $|c_1|$ that corresponds to the change in metamaterial response due to the coupling. We consider two cases: (i) detuning of 300 nm and (ii) no detuning between the metamaterial resonance and the transition. As observed in Figure 8b,c, in both the cases, increasing coupling increases the strength of the Fano dip in the spectrum. Furthermore, coupling enhancement is found to induce a strong lamb shift on the both sides of the dip and Rabi splitting is noticed when there is zero detuning. The profile of the Fano dip is found to be strongly dependent on the detuning which also agrees with the geometry dependent coupling in the actual system subject to heat induced perturbation, as observed in the experimental results of Figure 6.

3.4. Modulation Effect

We further compare the amount of resonance modulation achievable in the metamaterial structures when there is a large overlap of the modes with the transition. We fit the profiles by Lorentzian function with minimum residuals in **Figure 9** and define the modulation depth as illusrated. Please note that, such modulation is a direct outcome of the metamaterial induced transparency when the coupling of the vibrational mode with metamaterial mode occurs.[56] The induced transparency is also evident from the transmission measurements of the filter structure in Figure 5. It is clear that, the absorber structure provides 14 times better modulation when the transition occurs at 6.3 μm. The Lorentzian fitting also reveals a large degree of asymmetry as the absorption resonance couples with the vibrational transition. The relative difference defined as $1-I_{\text{fitting}}/I_{\text{experiment}}$ and plotted in Figure 9c clearly shows the enhanced asymmetry in the absorber structure around the transition wavelength. Such asymmetry is a direct outcome of the Fano like coupling in the system.

3.5. Relation to Strain Gradient

As discussed in the beginning, we attribute the excitation of the IR inactive mode to the large stress gradient of the high stress SiO_2 platform. To further verify, here, we provide the results in

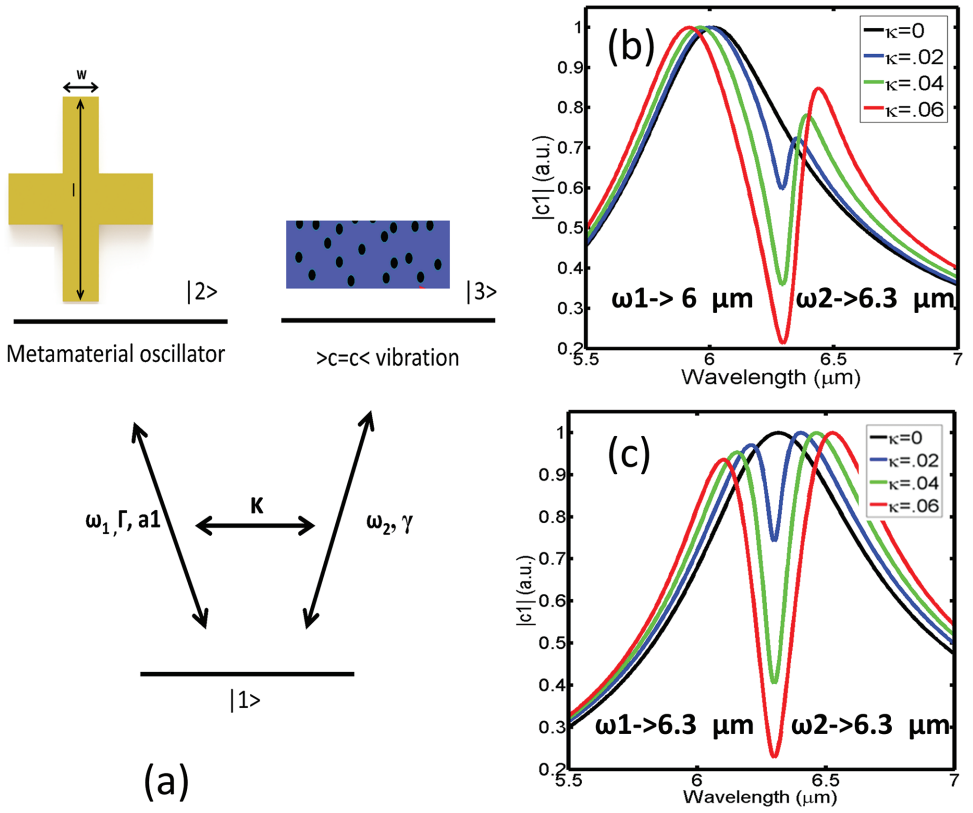

Figure 8. a) Toy model to analytically investigate the increasing coupling of the vibrational transition in the absence of heat induced stress and permittivity change. Effect of increasing coupling b) when detuning is 300 nm and c) when detuning is zero.

Figure 10a,b taken at 400 °C when the spacer of the absorber structure is replaced by Al_2O_3 and AlN, respectively. The stress (σ) which is created by the heating process, mainly originates from two different sources as formulated in the following equations

$$\sigma = \sigma_{th} + \sigma_i \tag{7}$$

$$\sigma_{th} = \frac{E}{1-\nu}\Delta\alpha\Delta T \tag{8}$$

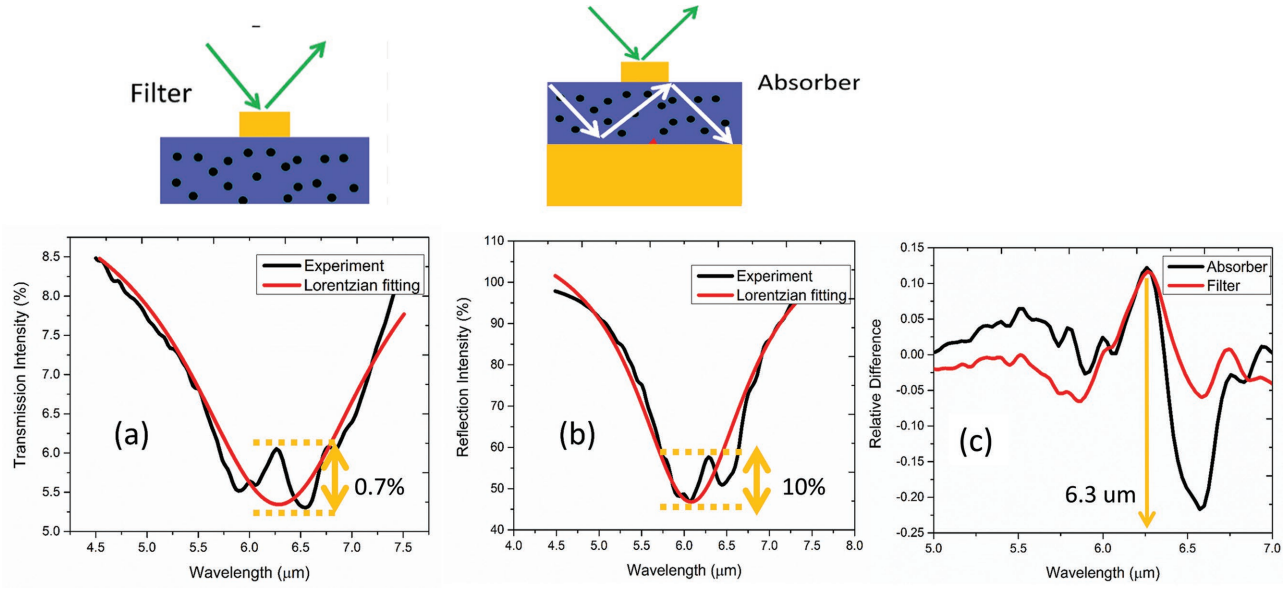

Figure 9. a) Lorentzian fitting of the modulated transmission dip (experiment) in C9 filter configuration. b) Lorentzian fitting of the modulated reflection dip (experiment) in C9 absorber configuration. The degree of modulation is marked by the orange double arrow. c) Comparison of relative difference in experiment between the absorber and filter configuration. The transition wavelength is marked by the orange arrow.

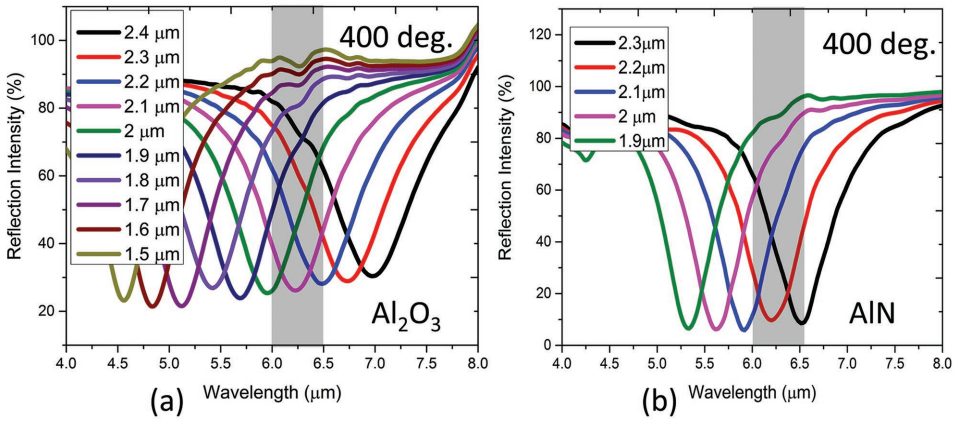

Figure 10. Reflection spectra as a function of length (l) at 400 °C. a) Al_2O_3 absorber. b) AlN absorber. Spacer thickness (d), width (w), and periodicity (p) are set at 200 nm, 283 nm, and 3.1 μm, respectively. The grey rectangle indicates the spectral location of the >C=C<modes.

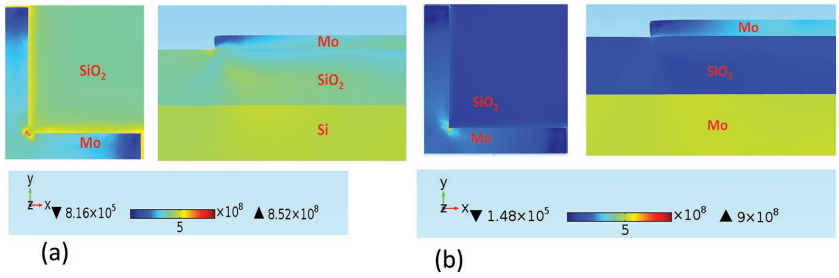

Figure 11. Thermal stress distribution obtained by FEM simulation of one-quarter of the layouts. a) Filter configuration (left-*xy* plane through the pattern; right-*xz* plane (cross section of the geometry) through the center of the pattern). b) Absorber configuration (left-*xy* plane through the pattern; right-*xz* plane (cross section of the geometry) through the center of the pattern. The stress gradient at the bottom interface in the absorber configuration can be four times larger than in the filter configuration assuming the Young's modulus and thermal expansion coefficient of silicon to be 179 GPa and 2.6×10^{-6} °C^{-1}, respectively.

$$\sigma_i = E\alpha\Delta T \tag{9}$$

Here, σ_{th} and σ_i are the residual and intrinsic stress, respectively. $\Delta\alpha$, E, ν, and ΔT are the TCE mismatch, Young's modulus, Poisson ratio, and temperature difference, respectively. Here, σ_{th} is the stress due to the TCE mismatch $\Delta\alpha$ between the adjacent layers whereas σ_i corresponds to stress due to the volumetric expansion of the respective layer when there is a positive temperature difference. Based on the mechanical properties listed in Tables 1 and 2, it can be found that the intrinsic stress gradient with the bottom Mo layer in SiO_2 platform can be 45 times larger than in the Al_2O_3 and AlN platform. Such stress gradient eventually leads to the strain gradient breaking the macroscopic symmetry of the dielectric and therefore, generates the net dipole moment.[57] The symmetry breaking in the thin film predominantly occurs at the bottom metal–dielectric interface. Previously, the SEM-EDS analysis has been able to detect the presence of carbon in the Al_2O_3 sample whereas no carbon signal was observed from the AlN sample. Under the valid approximation of similar magnitude of strain gradient in both the samples, we particularly observe the carbon induced feature in the Al_2O_3 device as marked by the grey rectangle in Figure 10a. Here, again we observe the suppression of the feature as the absorption resonance spectrally overlaps with it. Likewise in the SiO_2 platform, no strong modulation of the absorption resonance is observed at the maximum temperature of 400 °C. In **Figure 11**, we provide the FEM analysis of the stress in the filter and absorber configuration. As observed, larger stress gradient is generated at the interface of the bottom metal and spacer in the absorber structure based on SiO_2.

4. Conclusion

In summary, we demonstrate the coupling of IR inactive >C=C< vibration into the state-of-the-art metamaterial structures realized by the CMOS technology for the first time. The reversible nature of the stress engineered coupling may lead to a new class of functional device for detection in proteomics. We demonstrate stronger coupling of the vibration and enhanced modulation effect in the absorber structure which allows thin film interference when it is magnetically resonant. We further observe the suppression of the vibration when the cavity mode of the absorber strongly overlaps with the transition wavelength. Such unique behavior in coupled metamaterial system can possibly open up new routes for high temperature monitoring in rugged applications and/or efficient design of narrow band thermophotovoltaic device on the ubiquitous CMOS platform.

Supporting Information

Supporting Information is available from the Wiley Online Library or from the author.

Acknowledgements

The authors acknowledge the financial support from the research grant of, MOE/NUS, ARF-Tier 2 (MOE2012-T2-2-154,

NUS WBS: R-263-000-A59-112) "Monolithic integrated Si/AlN nanophotonics platform for optical NEMS and OEICs" and CRP-15th (NRF-CRP001-019)"Piezoelectric Photonics Using CMOS Compatible AlN Technology for Enabling The Next Generation Photonics ICs and Nanosensors" at the National University of Singapore, and the partial support by the National Natural Science Foundation of China under Grant No. 61474078 at NUS (Suzhou) Research Institute, Suzhou, China.

Received: September 23, 2016
Revised: October 17, 2016
Published online:

[1] M. Caldarola, P. Albella, E. Cortés, M. Rahmani, T. Roschuk, G. Grinblat, R. F. Oulton, A. V. Bragas, S. A. Maier, *Nat. Commun.* **2015**, *6*, 7915.
[2] M. Esfandyarpour, E. C. Garnett, Y. Cui, M. D. McGehee, M. L. Brongersma, *Nat. Nanotechnol.* **2014**, *9*, 542.
[3] A. Lenert, D. M. Bierman, Y. Nam, W. R. Chan, I. Celanović, M. Soljačić, E. N. Wang, *Nat. Nanotechnol.* **2014**, *9*, 126.
[4] D. Dregely, K. Lindfors, M. Lippitz, N. Engheta, M. Totzeck, H. Giessen, *Nat. Commun.* **2014**, *5*, 4354.
[5] K. Kumar, H. Duan, R. S. Hegde, S. C. W. Koh, J. N. Wei, J. K. W. Yang, *Nat. Nanotechnol.* **2012**, *7*, 557.
[6] C. Della Giovampaola, N. Engheta, *Nat. Mater.* **2014**, *13*, 1115.
[7] S. Bidault, A. Devilez, P. Ghenuche, B. Stout, N. Bonod, J. Wenger, *ACS Photonics* **2016**, *3*, 895.
[8] W. Zhu, K. B. Crozier, *Nat. Commun.* **2014**, *5*, 5228.
[9] C. Cao, J. Zhang, X. Wen, S. L. Dodson, N. T. Dao, L. M. Wong, S. Wang, S. Li, A. T. Phan, Q. Xiong, *ACS Nano* **2013**, *7*, 7583.
[10] Y. Liu, Y. Park, S. E. Lee, *Appl. Phys. Lett.* **2016**, *109*, 13109.
[11] R. Singh, N. Zheludev, *Nat. Photonics* **2014**, *8*, 679.
[12] L. Cong, N. Xu, D. R. Chowdhury, M. Manjappa, C. Rockstuhl, W. Zhang, R. Singh, *Adv. Opt. Mater.* **2016**, *4*, 252.
[13] F. Yi, M. Ren, J. C. Reed, H. Zhu, J. Hou, C. H. Naylor, A. T. C. Johnson, R. Agarwal, E. Cubukcu, *Nano Lett.* **2016**, *16*, 1631.
[14] J. H. Son, B. Cho, S. Hong, S. H. Lee, O. Hoxha, A. J. Haack, L. P. Lee, *Light: Sci. Appl.* **2015**, *4*, e280.
[15] D. Hasan, C. P. Ho, P. Pitchappa, C. Lee, *ACS Photonics* **2015**, *2*, 890.
[16] D. Hasan, C. P. Ho, P. Pitchappa, B. Yang, C. Yang, C. Lee, *Sci. Rep.* **2016**, *6*, 22227.
[17] D. Hasan, C. P. Ho, C. Lee, *Adv. Opt. Mater.* **2016**, *4*, 943.
[18] X. Xu, H. Li, D. Hasan, R. S. Ruoff, A. X. Wang, D. L. Fan, *Adv. Funct. Mater.* **2013**, *23*, 4332.
[19] X. Xu, D. Hasan, L. Wang, S. Chakravarty, R. T. Chen, D. L. Fan, A. X. Wang, *Appl. Phys. Lett.* **2012**, *100*, 191114.
[20] D. Hasan, M. S. Alam, *J. Lightwave Technol.* **2014**, *32*, 1434.
[21] F. Ren, J. Campbell, D. Hasan, X. Wang, G. L. Rorrer, A. X. Wang, in *CLEO*, OSA, Washington **2013**, p. CTh3I.4.
[22] D. Hasan, J. Wang, C. Lee, in *Proc. IEEE*, IEEE, Piscataway, NJ, USA **2016**, pp. 234–237.
[23] D. Hasan, C. P. Chong Pei Ho, P. Pitchappa, C. Chengkuo Lee, in *Proc. IEEE*, IEEE, Piscataway, NJ, USA **2015**, pp. 1–2.
[24] A. Kuzyk, R. Schreiber, H. Zhang, A. O. Govorov, T. Liedl, N. Liu, *Nat. Mater.* **2014**, *13*, 862.
[25] D. Chanda, K. Shigeta, S. Gupta, T. Cain, A. Carlson, A. Mihi, A. J. Baca, G. R. Bogart, P. Braun, J. A. Rogers, *Nat. Nanotechnol.* **2011**, *6*, 402.
[26] F. De Angelis, M. Malerba, M. Patrini, E. Miele, G. Das, A. Toma, R. P. Zaccaria, E. Di Fabrizio, *Nano Lett.* **2013**, *13*, 3553.
[27] C. P. Chong Pei Ho, P. Pitchappa, P. Kropelnicki, J. Jian Wang, Y. Yuandong Gu, C. Chengkuo Lee, *IEEE J. Sel. Top. Quantum Electron.* **2014**, *20*, 94.
[28] C. P. Ho, P. Pitchappa, P. Kropelnicki, J. Wang, H. Cai, Y. Gu, C. Lee, *Opt. Lett.* **2015**, *40*, 2743.
[29] P. Pitchappa, C. Pei Ho, P. Kropelnicki, N. Singh, D.-L. Kwong, C. Lee, *Appl. Phys. Lett.* **2014**, *104*, 201114.
[30] P. Pitchappa, M. Manjappa, C. P. Ho, R. Singh, N. Singh, C. Lee, *Adv. Opt. Mater.* **2016**, *4*, 540.
[31] P. Pitchappa, C. P. Ho, L. Cong, R. Singh, N. Singh, C. Lee, *Adv. Opt. Mater.* **2016**, *4*, 391.
[32] J. D. Caldwell, L. Lindsay, V. Giannini, I. Vurgaftman, T. L. Reinecke, S. A. Maier, O. J. Glembocki, *Nanophotonics* **2015**, *4*, 44.
[33] M. Freitag, T. Low, W. Zhu, H. Yan, F. Xia, P. Avouris, *Nat. Commun.* **2013**, *4*, 486.
[34] Z. Chen, J. Guo, P. Ong, *Appl. Phys. Lett.* **2003**, *83*, 2151.
[35] D. A. Derek, A. Long, *The Raman Effect: A Unified Treatment of the Theory of Raman Scattering by Molecules*, Wiley, Chichester, UK **2002**.
[36] R. J. Anderson, D. J. Bendell, P. W. Groundwater, R. J. Anderson, D. J. Bendell, P. W. Groundwater, *Organic Spectroscopic Analysis*, Royal Society of Chemistry, Cambridge, UK **2004**.
[37] J. H. Kaufman, S. Metin, D. D. Saperstein, *Phys. Rev. B* **1989**, *39*, 13053.
[38] M. Lee, H. Jeon, S. Kim, *Nano Lett.* **2015**, *15*, 3358.
[39] S. Philip J., K. Mark, *J. Vac. Sci. Technol.* **1993**, *11*, 2652.
[40] P. Dozoretz, Y. Gu, US Patent, *US6197119B1*, **1999**.
[41] C. E. Viana, A. N. R. da Silva, N. I. Morimoto, O. Bonnaud, *Braz. J. Phys.* **2001**, *31*, 299.
[42] M. Reichenbächer, J. Popp, in *Challenges in Molecular Structure Determination*, Springer, Berlin Heidelberg, Germany **2012**, pp. 63–143.
[43] S. Shimomura, Y. Fujii, S. Nozawa, K. Kikuchi, Y. Achiba, I. Ikemoto, *Solid State Commun.* **1993**, *85*, 471.
[44] C. Schriever, C. Bohley, J. Schilling, R. B. Wehrspohn, *Materials* **2012**, *5*, 889.
[45] A. S. Paipetis, *tress induced changes in the Raman Spectrum of Carbon Nanostructures and their Composites,* Springer, The Netherlands **2013**, pp. 185–217.
[46] W. Vogel, D.-G. Welsch, S. Wallentowitz, *Quantum Optics*, Wiley-VCH, Weinheim, Germany **2006**.
[47] B. Lahiri, A. Z. Khokhar, R. M. De La Rue, S. G. McMeekin, N. P. Johnson, *Opt. Express* **2009**, *17*, 1107.
[48] B. G. Varshal, V. N. Denisov, B. N. Mavrin, V. G. Podobedov, K. Y. Sterin, *Rep. Phys. Math.* **1983**, *9*, 513.
[49] S. D. Emami, R. Penny, H. A. Abdul Rashid, W. S. Mohammed, B. M. A. Rahman, *Reviews in Plasmonics 2015*, Springer, New York **2016**, pp. 191–224.
[50] M. Bosman, L. Zhang, H. Duan, S. F. Tan, C. A. Nijhuis, C. Qiu, J. K. W. Yang, *Sci. Rep.* **2014**, *4*, 2231.
[51] H.-T. Chen, *Opt. Express* **2012**, *20*, 7165.
[52] A. Vora, J. Gwamuri, N. Pala, A. Kulkarni, J. M. Pearce, D. Ö. Güney, *Sci. Rep.* **2014**, *4*, 2.
[53] D. J. Shelton, I. Brener, J. C. Ginn, M. B. Sinclair, D. W. Peters, K. R. Coffey, G. D. Boreman, *Nano Lett.* **2011**, *11*, 2104.
[54] H. A. Haus, W. Huang, *Proc. IEEE* **1991**, *79*, 1505.
[55] M. V. Rybin, S. F. Mingaleev, M. F. Limonov, Y. S. Kivshar, *Sci. Rep.* **2016**, *6*, 20599.
[56] L. V. Brown, X. Yang, K. Zhao, B. Y. Zheng, P. Nordlander, N. J. Halas, *Nano Lett.* **2015**, *15*, 1272.
[57] J. Laconte, D. Flandre, J.-P. Raskin, *Micromachined Thin-Film Sensors for SOI-CMOS Co-Integration*. Springer, New York, **2006**, pp. 47–103.